Chinese Chemical Letters 36 (2025) 110279

Contents lists available at ScienceDirect

Chinese Chemical Letters

journal homepage: www.elsevier.com/locate/cclet

Boosted solar water oxidation steered by atomically precise alloy nanocluster

Xian Yan[a], Huawei Xie[b], Gao Wu[a], Fang-Xing Xiao[a,c,*]

[a] College of Materials Science and Engineering, Fuzhou University (New Campus), Minhou 350108, China
[b] Department of Forensic Science, The Engineering Research Center, Fujian Police College, Fuzhou 350002, China
[c] State Key Laboratory of Structural Chemistry, Fujian Institute of Research on the Structure of Matter, Chinese Academy of Sciences, Fuzhou 350002, China

ARTICLE INFO

Article history:
Received 7 June 2024
Revised 16 July 2024
Accepted 16 July 2024
Available online 17 July 2024

Keywords:
Alloy nanoclusters
Self-assembly
Charge transport
Photoanodes
Photoelectrochemical water oxidation

ABSTRACT

Atomically precise metal nanoclusters (NCs) have been deemed as a new generation of metal nanomaterials in the field of solar energy conversion due to their unique atomic stacking manner, quantum confinement effects, light-harvesting capability and multitude of active sites. Nonetheless, wide-spread application of monometallic NCs is blocked by the ultrashort carrier lifespan, uncontrollable charge transport pathway, and light-induced poor stability, impeding the construction of robust and stable metal NC-based photosystems. Herein, we report the fabrication of stable alloy ($Au_{1-x}Pt_x$) NCs photosystem, for which tailor-made negatively charged L-glutathione (GSH)-capped $Au_{1-x}Pt_x$ NCs as the building blocks are controllably deposited on the $BiVO_4$ (BVO) by a self-assembly approach for steering enhanced light absorption and interfacial charge transfer over alloy NCs-based photoanodes ($Au_{1-x}Pt_x$/BVO). The self-assembled $Au_{1-x}Pt_x$/BVO composite photoanode exhibits the significantly enhanced photoelectrochemical water oxidation performances compared with pristine BVO and Au_x/BVO photoanodes, which is caused by the Pt atom doping into the Au_x NCs for elevating photosensitivity and boosting the stability. The synergy of Au and Pt atoms in alloy NCs protects the gold core from rapid oxidation, improving the photostability and accelerating the surface charge transfer kinetics. Our work would significantly inspire ongoing interest in unlocking the charge transport characteristics of atomically precise alloy NCs for solar energy conversion.

Atomically precise metal nanoclusters (NCs) have been considered to be a new generation of photosensitizers because of peculiar atom-stacking mode, quantum confinement effect, and enriched catalytic active sites [1-4]. However, utilization of metal NCs is retarded by the ultrashort charge lifetime, uncontrollable charge transport pathway, and poor stability [5-8]. Although some metal NCs-based photosystems have been reported, they are mainly limited to monometallic NCs [9-11]. It has been reported that doping foreign atoms into pristine monometallic NCs favors enhancing the stability and catalytic activity owing to tunable electronic structure modulation [12,13]. Furthermore, optical properties of metal NCs can also be tailored by heterometal atom substitution [14-16]. This signifies that alloy NCs show great potential for exploring photoelectrochemical (PEC) systems for water oxidation [17-21].

Bismuth vanadate ($BiVO_4$) is considered as an emerging photoanode considering its beneficial light absorption, high oxidation, and enriched active sites [22,23]. However, $BiVO_4$-involved PEC systems suffer from rapid charge recombination and sluggish charge transport kinetics. Therefore, it remains challenging to construct robust and stable $BiVO_4$ photoanodes for PEC water oxidation. Combining $BiVO_4$ with alloy NCs may offers an applicable route to solve the bottlenecks of $BiVO_4$ given their favorable energy level alignment that facilitates the directional charge transfer. Besides, intrinsic photosensitization capability of alloy NCs may also increase the carrier intensity and enhance the charge separation of composite photosystems [24-26]. As such, rationally coupling alloy NCs with $BiVO_4$ would create novel high-efficiency PEC photosystems.

Herein, L-glutathione (GSH)-capped gold-platinum alloy NCs ($Au_{1-x}Pt_x$@GSH) were electrostatically self-assembled on the $BiVO_4$ (BVO) substrate to construct $Au_{1-x}Pt_x$/BVO hybrid photoanode for PEC water oxidation. It was found that alloy NCs surpass the homo-metallic NCs in promoting the photosensitization of $BiVO_4$, while reinforcing the photostability. The $Au_{1-x}Pt_x$/BVO hybrid photoanode exhibits the considerably improved PEC water oxidation activities compared with BVO and Au_x/BVO counterparts, which is caused by the Pt atom doping into the Au_x NCs for elevating the photosensitivity and boosting the stability. This work unveils the

* Corresponding author.
E-mail address: fxxiao@fzu.edu.cn (F.-X. Xiao).

https://doi.org/10.1016/j.cclet.2024.110279
1001-8417/

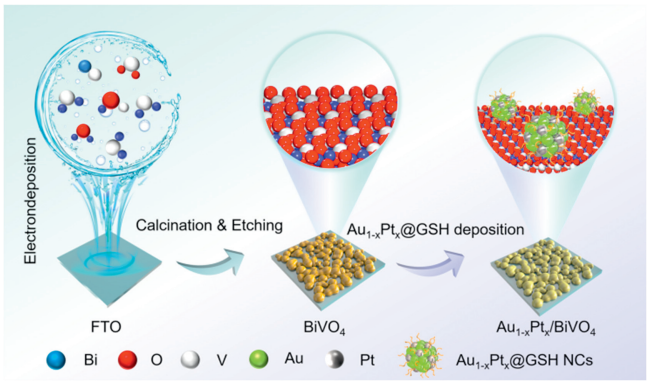

Scheme 1. Schematic diagram depicting the self-assembly of $Au_{1-x}Pt_x/BiVO_4$ photoanodes.

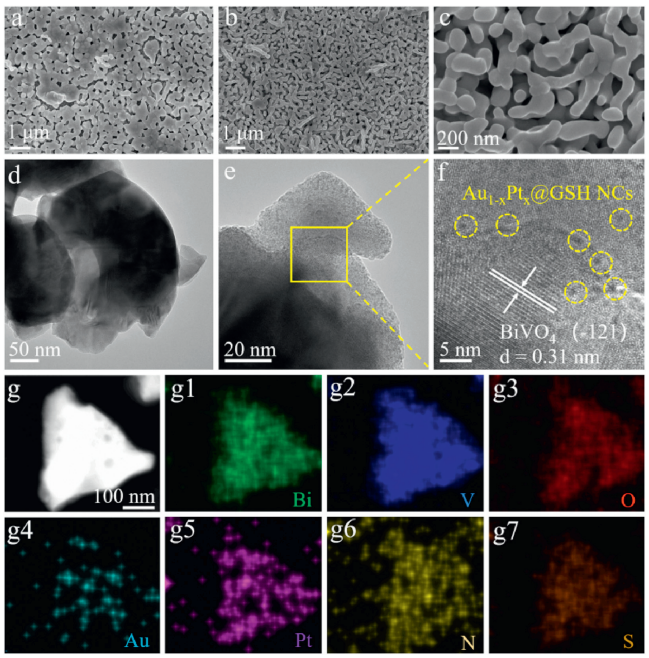

Fig. 1. FESEM images of (a) BVO and (b, c) $Au_{1-x}Pt_x$-4/BVO. TEM and high-resolution TEM images of (d-f) $Au_{1-x}Pt_x$-4/BVO with (g, g1-g7) elemental mapping results.

charge transport characteristics of alloy NCs-based photosystems for solar energy conversion.

Scheme 1 shows the flowchart for fabricating $BiVO_4$ and alloy NCs/$BiVO_4$ composite photoanodes. Firstly, $BiVO_4$ photoelectrode was prepared by an electrochemical deposition method. Subsequently, tailor-made $Au_{1-x}Pt_x$ NCs were electrostatically deposited on the BVO surface. Notably, atomically precise alloy NCs are capped by GSH ligands which contains various deprotonated carboxyl groups (-COO-), generating the negatively charged surface, as evidenced by the zeta potential result (Fig. S1b in Supporting information). This favors the deposition of alloy NCs on the BVO substrate *via* electrostatic interaction at ambient conditions.

As shown in Fig. 1a, BVO substrate shows a porous nanostructure. As displayed in Figs. 1b and c, the morphology of BVO does not change apparently after loading $Au_{1-x}Pt_x$ NCs, and it is difficult to observe the deposition of $Au_{1-x}Pt_x$ NCs on the BVO surface in the SEM image of $Au_{1-x}Pt_x$-4/BVO (abbreviated as AuPt-4/BVO), which is mainly caused by the ultra-small size of alloy NCs (~1.35 nm) (Figs. S1c and d in Supporting information). To determine the distribution of alloy NCs in $Au_{1-x}Pt_x$-4/BVO, TEM (Fig. 1d) and HRTEM (Figs. 1e and f) images were probed. As exhibited in Fig. 1f, a large quantity of $Au_{1-x}Pt_x$ NCs are uniformly deposited on the BVO substrate surface. Furthermore, the crystal structure of the BVO is well defined with a distinguishable lattice stripe of ~0.31 nm, which corresponds to the $(\bar{1}21)$ crystal plane of monoclinic scheelite $BiVO_4$ [27]. However, no lattice fringe of $Au_{1-x}Pt_x$ NCs is visualized, which is due to the unique atomic stacking mode of alloy NCs. Moreover, the uniform deposition of $Au_{1-x}Pt_x$ NCs on the BVO can also be corroborated by the elemental mapping results of $Au_{1-x}Pt_x$-4/BVO. Figs. 1g and g1-g7 show the distribution pattern of Bi, V, O, S, N, Au and Pt signals for $Au_{1-x}Pt_x$-4/BVO heterostructure, wherein N & S signals originated from GSH ligand and Au & Pt signals from $Au_{1-x}Pt_x$-4 NCs are uniformly distributed the entire framework of BVO substrate.

As displayed in Fig. 2a, XRD results of $Au_{1-x}Pt_x$-4/BVO, $Au_{1-x}Pt_x$-3/BVO, Au_x/BVO and BVO are similar with diffraction peaks accurately indexed to the monoclinic scheelite $BiVO_4$ (JCPDS No. 14–0688). The peaks from FTO are indicated by black dots. No peaks assignable to $Au_{1-x}Pt_x$@GSH and Au_x@GSH are observed in the XRD patterns of nanocomposites, which is due to the low deposition amount of metal NCs [28]. Similarly, Raman spectra (Fig. S2 in Supporting information) also exhibit the featured $BiVO_4$ peaks without the peaks of $Au_{1-x}Pt_x$@GSH and Au_x@GSH. As shown in Fig. 2b and Table S1 (Supporting information), FTIR result of blank BVO demonstrates the peaks at 3426.1, 703 & 1057 and 476 cm^{-1}, which are corresponding to the -OH group, V-O and O-Bi bonds from BVO, respectively [29]. In comparison with FTIR spectrum of BVO, besides the vibration band of BVO, another two peaks at 2920 and 2850 cm^{-1} are seen in the FTIR spectra of Au_x/BVO, $Au_{1-x}Pt_x$-3/BVO and $Au_{1-x}Pt_x$-4/BVO, which correspond to the -CH_2 group from the GSH ligands of metal NCs [19], confirming the successful deposition of Au_x@GSH NCs, $Au_{1-x}Pt_x$-3@GSH NCs and $Au_{1-x}Pt_x$-4@GSH NCs on the BVO substrate [19]. As shown in Fig. 2c, DRS results of BVO, Au_x/BVO, $Au_{1-x}Pt_x$-3/BVO and $Au_{1-x}Pt_x$-4/BVO indicate that their light absorption band edge is located at 480 nm, which originates from the band-gap-photoexcitation of BVO substrate. This suggests that Au_x@GSH NCs, $Au_{1-x}Pt_x$-3@GSH NCs and $Au_{1-x}Pt_x$-4@GSH NCs deposition on the BVO does not alter the optical properties of metal NCs/BVO composite photoanodes, which is due to the overlapping light absorption of BVO with metal NCs in the visible spectrum region. The result is reasonable considering the UV–vis absorption spectra of Au_x@GSH NCs, $Au_{1-x}Pt_x$-3@GSH NCs and $Au_{1-x}Pt_x$-4@GSH NCs (Fig. S1a in Supporting information). Furthermore, the slight enhancement in light absorption within the 500–800 nm can be attributed to the inherent light absorption properties of BVO. Moreover, band gap of BVO by transformed plots according to the Kubelka-Munk function *vs.* the energy of light is roughly calculated to be ~2.46 eV (Fig. S3 in Supporting information). As shown in Fig. S4 (Supporting information), Au_x@GSH and $Au_{1-x}Pt_x$-4@GSH NCs demonstrate the similar light absorption profile, suggesting that Pt atom doping fails to alter the optical properties of Au_x@GSH NCs.

As exhibited in Fig. S5a (Supporting information), survey spectrum of $Au_{1-x}Pt_x$-4/BVO demonstrates the presence of Bi 4f, V 2p, O 1s, N 1s, Au 4f, and Pt 4f signals, among which Au 4f, O 1s, N 1s and Pt 4f elements arise from $Au_{1-x}Pt_x$-4@GSH NCs. As shown in Figs. 2d and e, high-resolution V 2p and Bi 4f spectra of $Au_{1-x}Pt_x$-4/BVO (II) and BVO (I) correspond to the Bi^{3+} and V^{5+}species [30], respectively. The result implies that $Au_{1-x}Pt_x$ NCs deposition does not change the elemental chemical states of BVO substrate. As revealed in Fig. 2f, the peaks at *ca.* 529.7, 531.13 and 532.4 eV in the high-resolution O 1s spectrum of $Au_{1-x}Pt_x$-4/BVO (II) are attributed to the Bi-O, -OH and carboxyl group (C=O) [31], respectively. Compared with the high-resolution O 1s spectrum of BVO (I), the appearance of carboxyl group in $Au_{1-x}Pt_x$-4/BVO strongly verifies the self-assembly of $Au_{1-x}Pt_x$-4 NCs on the BVO substrate. It should be emphasized that the characteristic peaks of Bi 4f, V 2p and O

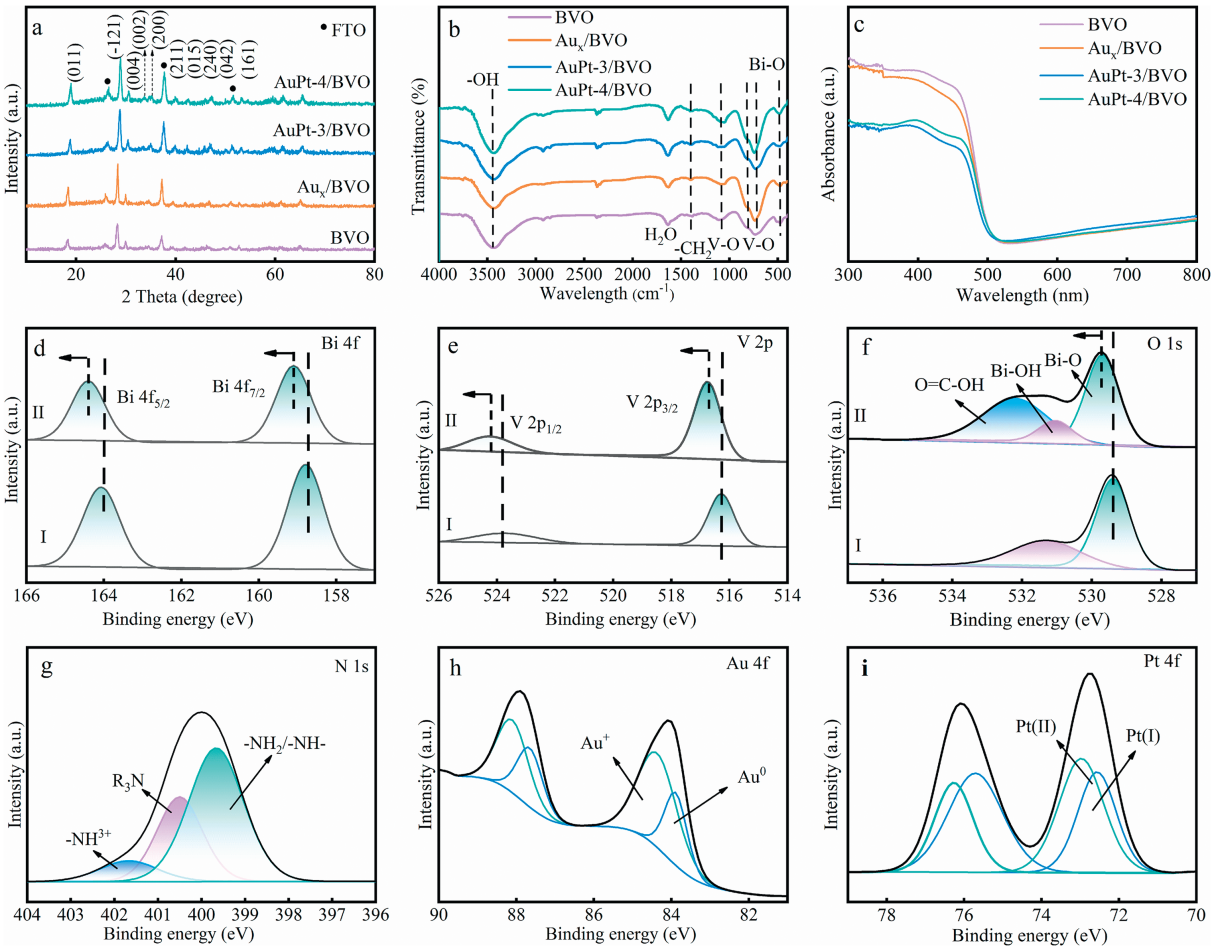

Fig. 2. (a) XRD patterns, (b) FTIR spectra and (c) DRS results of $Au_{1-x}Pt_x$-4/BVO, $Au_{1-x}Pt_x$-3/BVO, Au_x/BVO and BVO. High-resolution (d) Bi 4f, (e) V 3p, (f) O 1s, (g) N 1s, (h) Au 4f and (i) Pt spectra of (I) BVO and (II) $Au_{1-x}Pt_x$-4/BVO.

1s spectra for $Au_{1-x}Pt_x$/BVO markedly move to the higher energy level compared with blank BVO substrate [32]. These results evidence the robust interaction between $Au_{1-x}Pt_x$ NCs and BVO, resulting in the efficient electron transfer at the $Au_{1-x}Pt_x$ /BVO hybrid interface. High-resolution N 1s spectra (Fig. 2g) of $Au_{1-x}Pt_x$-4/BVO demonstrate the peaks at 399.67, 400.05 and 401.67 eV, which are corresponding to the -NH_2/-NH-, -NH^{3+} and N–C=O species from the GSH ligands of $Au_{1-x}Pt_x$ NCs [19,28], respectively. Consistently, as displayed in Fig. S5b (Supporting information), the peaks at 284.6, 286.4 and 288.08 eV in the high-resolution C 1s spectrum of $Au_{1-x}Pt_x$-4/BVO are indexed to the C–H, C–OH/C–O-C, and-COO- species from the GSH ligands capped on the surface of $Au_{1-x}Pt_x$ NCs [19,28]. Fig. 2h shows two 4f peaks in the high-resolution Au 4f spectra of $Au_{1-x}Pt_x$-4/BVO, which correspond to the Au^0 and Au^+ species in the $Au_{1-x}Pt_x$-4@GSH NCs, once again confirming the successful attachment of metal NCs on the BVO substrate. For the high-resolution Pt 4f spectrum, there are two characteristic peaks at 72.8 (Pt $4f_{7/2}$) and 76.1 eV (Pt $4f_{5/2}$), respectively (Fig. 2i), and the $4f_{7/2}$ peak can be further divided into two components with binding energy of 72.57 and 73.0 eV, belonging to the Pt(I) and Pt(II) species, respectively. The results manifest that almost all the Pt atoms form Pt-S bonds with the sulfhydryl groups on GSH ligand and are distributed on the peripheral surface of the nucleus. The above results indicate that $Au_{1-x}Pt_x$-4@SSH NCs are mainly composed of Au(0) in the core and Au(I), Pt(I) and Pt(II) on the surface [33-35]. Therefore, we deduce the structural model of $Au_{1-x}Pt_x$@GSH NCs as shown in Fig. S6 (Supporting information). For comparison, Table S2 (Supporting information) summarizes the chemical bonding species *versus* binding energy for $Au_{1-x}Pt_x$-4/BVO heterostructure.

PEC water oxidation performances of the photoanodes are probed under simulated solar light irradiation. The loading amount of metal NCs was mediated by the dipping time. As shown in Fig. S7a (Supporting information), photocurrents of metal NCs/BVO photoanodes are substantially affected by the dipping time of BVO in metal NCs aqueous solution. Specifically, photocurrents of $Au_{1-x}Pt_x$-4/BVO-X (X = 4, 6, 8 h) demonstrate no apparent change and tends to saturate as the dipping time increases from 2 h to 6 h, based on which the optimal dipping time of 2 h was thus determined and utilized to fabricate other counterparts. As shown in Fig. S7b (Supporting information), alloy metal NCs photosensitized BVO photoanodes demonstrate the optimal PEC performance when the molar ratio of Au to Pt is controlled to be 1:0.8, and thus $Au_{1-x}Pt_x$-4/BVO heterostructure was harnessed as the optimal sample for the following systematic investigation.

Fig. 3a shows that linear sweep voltammetry (LSV) results of metal NCs/BVO composite photoanodes are closely related to the Pt doping. The boosted photocurrents of $Au_{1-x}Pt_x$-4/BVO and $Au_{1-x}Pt_x$-3/BVO relative to BVO reveals the crucial role of $Au_{1-x}Pt_x$@GSH NCs in boosting the PEC performances. Among them, $Au_{1-x}Pt_x$-4/BVO and $Au_{1-x}Pt_x$-3/BVO deliver a photocurrent of 1.6 and 1.3 mA/cm^2 at 1.23 V *vs.* RHE, representing a two-fold enhancement compared with blank BVO (0.8 mA/cm^2). This is ascribed to the photosensitization effect of $Au_{1-x}Pt_x$@GSH NCs and formation of applicable type II energy level alignment between BVO and $Au_{1-x}Pt_x$@GSH NCs, which improves the electrons transfer

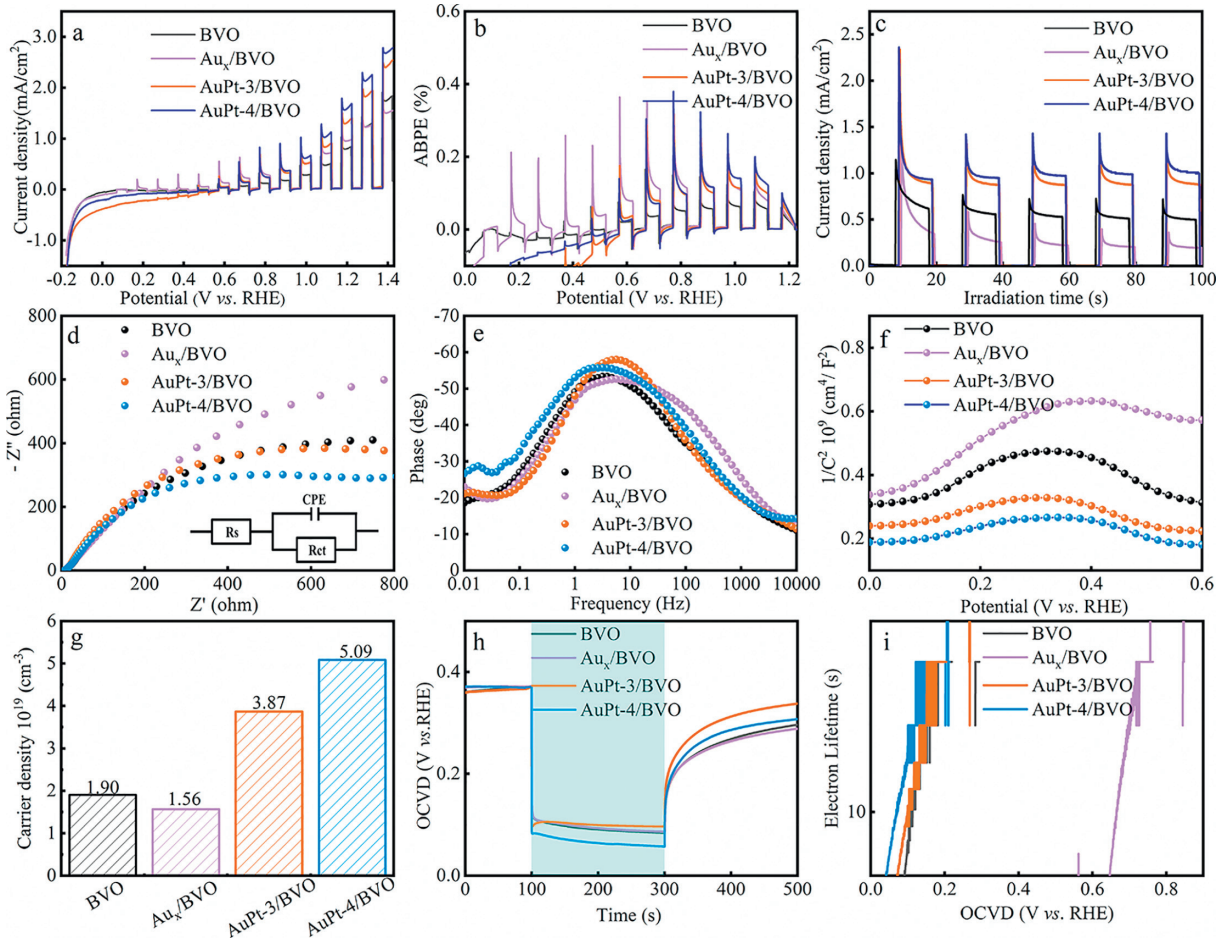

Fig. 3. PEC water oxidation activities of BVO, Au_x/BVO, $Au_{1-x}Pt_x$-3/BVO and $Au_{1-x}Pt_x$-4/BVO heterostructures under simulated solar light irradiation (AM 1.5G) including (a) LSV, (b) ABPE, (c) transient photocurrents (*I-t*) (1.23 V *vs.* RHE), (d) EIS results, (e) Bode curves, (f) M-S plots, (g) charge density (N_d), (h) OCVD, and (i) electron lifetime (τ_n).

from $Au_{1-x}Pt_x$@GSH NCs to BVO. It is noteworthy that Au_x@GSH NCs photosensitized BVO as a control sample exhibits gradually decreased photocurrent, which is related to the poor stability of Au_x@GSH NCs. Based on the LSV results, applied bias photon-to-current efficiency (ABPE, η) results of the photoanodes were calculated. As displayed in Fig. 3b, $Au_{1-x}Pt_x$-4/BVO shows the optimal η of 0.17%, followed by $Au_{1-x}Pt_x$-3/BVO, BVO and Au_x/BVO with η of 0.16%, 0.06% and 0.13%, respectively. The result is consistent with the LSV results, and it is after 1.0 V *vs.* RHE that instability of metal NCs starts to exerts a profound effect on the overall photocurrent magnitude of the metal NCs/BVO composite photoanode. Fig. 3c shows that $Au_{1-x}Pt_x$-4/BVO demonstrates the most enhanced photocurrent compared with BVO, $Au_{1-x}Pt_x$-3/BVO, and Au_x/BVO counterparts, indicative of its most efficient charge separation.

Electrochemical impedance spectroscopy (EIS) results under light irradiation (AM 1.5G) were probed to evaluate the interfacial charge transport resistance of photoelectrodes [36]. As displayed in Fig. 3d, $Au_{1-x}Pt_x$-4/BVO (890.7 ohm) shows the smallest semicircular arc radius under light irradiation relative to BVO (1157 ohm), $Au_{1-x}Pt_x$-3/BVO (1100 ohm), and Au_x/BVO (1691 ohm), manifesting its lowest interfacial charge transfer resistance, which agrees with the LSV and *I-t* results. In addition, Bode plot representing the frequency response of the PEC system was probed to assess the electron lifetime (τ_e) of photoelectrodes. As shown in Fig. 3e, τ_e of $Au_{1-x}Pt_x$-4/BVO demonstrates the longest electron lifetime of 0.05 s, which is longer than those of $Au_{1-x}Pt_x$-3/BVO (0.0283 s), Au_x/BVO (0.0283 s) and BVO (0.0416 s). Mott-Schottky (M-S) results were probed to unveil the charge carrier density (Fig. 3f) [37]. As displayed in Fig. 3g, carrier density (N_d) of $Au_{1-x}Pt_x$-4/BVO, $Au_{1-x}Pt_x$-3/BVO, Au_x/BVO and BVO are determined as 5.09×10^{19}, 3.87×10^{19}, 1.56×10^{19} and 1.90×10^{19} cm^{-3}, respectively. Consistently, $Au_{1-x}Pt_x$-4/BVO still demonstrates the optimal carrier density followed by $Au_{1-x}Pt_x$-3/BVO, BVO and Au_x/BVO. As reflected by Fig. 3h, $Au_{1-x}Pt_x$-4/BVO demonstrates the largest photovoltage. Additionally, electron lifetime of photoelectrodes calculated by the photovoltage is shown in Fig. 3i, which suggests that $Au_{1-x}Pt_x$-4/BVO demonstrates the longest electron lifetime, indicating its most efficient charge separation efficiency [38].

To highlight the key role of $Au_{1-x}Pt_x$@GSH NCs in improving the charge separation efficiency of composite photoanodes, charge injection (η_{inj}) and separation efficiency (η_{sep}) of $Au_{1-x}Pt_x$-4/BVO were further tested. As displayed in Fig. 4a, based on the LSV results of $Au_{1-x}Pt_x$-4/BVO and BVO with and without adding sodium sulfite (Na_2SO_3), η_{inj} and η_{sep} of the photoanode were calculated. As shown in Fig. 4b, η_{sep} of $Au_{1-x}Pt_x$-4/BVO is almost twice as much as that of BVO. The higher charge separation efficiency promotes the water oxidation reaction and improves the PEC performance. It is noteworthy that $Au_{1-x}Pt_x$-4/BVO also demonstrate improved η_{inj} relative to pure BVO (Fig. 4c), which implies that the $Au_{1-x}Pt_x$ NCs possess a favorable photo-sensitizing effect as well as advantageous energy level alignment between BVO and $Au_{1-x}Pt_x$@GSH NCs [39]. Stability of $Au_{1-x}Pt_x$/BVO photoanode was probed. As shown in Fig. 4d, $Au_{1-x}Pt_x$-4/BVO demonstrates the favorable photostability without adding additional sacrificial reagent with small photocurrent decay, verifying the good stability of $Au_{1-x}Pt_x$ NCs. This is caused by the heteroatomic metallic Pt atom

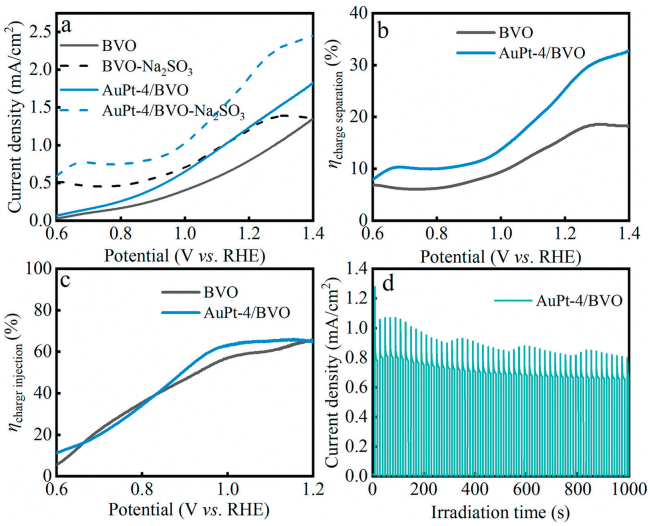

Fig. 4. (a) LSV results of $Au_{1-x}Pt_x$-4/BVO with (dash line) and without (solid line) adding Na_2SO_3 (0.01 mol/L) in Na_2SO_4 aqueous solution (0.5 mol/L, pH 6.69) under simulated solar light irradiation (AM 1.5G). Charge (b) separation and (c) injection efficiency of $Au_{1-x}Pt_x$-4/BVO. (d) Photostability of $Au_{1-x}Pt_x$-4/BVO in Na_2SO_4 aqueous solution under simulated sunlight irradiation (AM 1.5G).

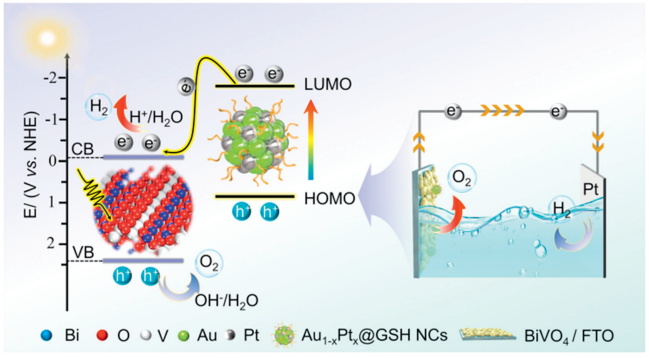

Scheme 2. Schematic illustration of the PEC water oxidation mechanism of $Au_{1-x}Pt_x$-4/BVO heterostructure.

doping in the motif of Au_x NCs. The synergy of gold and platinum atoms protect the gold core from rapid oxidation, improving the photostability and accelerating the surface charge transfer kinetics. This speculation is proved by the SEM image of $Au_{1-x}Pt_x$-4/BVO after reaction. As shown in Fig. S8 (Supporting information), no agglomeration of $Au_{1-x}Pt_x$-4@GSH NCs on the $Au_{1-x}Pt_x$-4/BVO surface is observed, which evidences the good photostability of alloy NCs.

PEC water splitting mechanism of $Au_{1-x}Pt_x$/BVO photoanode was depicted in Scheme 2. According to the previous work [35], Au_x@GSH NCs are featured by HOMO-LUMO gap and are able to serve as *quasi*-semiconductor with small bandgap. Based on the UV–vis absorption (Fig. S9a in Supporting information) and CV results (Fig. S9b in Supporting information), HOMO and LUMO levels of Au_x@GSH NCs were determined as −2.13 eV *vs.* NHE and 0.63 V *vs.* NHE, respectively. Similarly, HOMO and LUMO levels of $Au_{1-x}Pt_x$-4@GSH NCs were determined as −1.78 eV *vs.* NHE and 0.98 V *vs.* NHE, respectively (Figs. S9d and e in Supporting information). The diagrams showing the HOMO and LUMO levels of Au_x@GSH and $Au_{1-x}Pt_x$-4@GSH NCs are shown in Figs. S9c and f (Supporting information), from which it is apparent that Pt atom doping changes the HOMO position of Au_x@GSH NCs, that is, HOMO potential of Au_x@GSH NCs is much higher than that of $Au_{1-x}Pt_x$-4@GSH NCs. Thus, PEC water oxidation mechanism of $Au_{1-x}Pt_x$-4/BVO photoanode is proposed and illustrated in Scheme 2. When $Au_{1-x}Pt_x$-4/BVO was irradiated by simulated sunlight, $Au_{1-x}Pt_x$-4@GSH NCs are photoexcited to produce electrons and holes in the LUMO and HOMO, respectively. It has been well established that LUMO potential of $Au_{1-x}Pt_x$-4@GSH NCs is more negative than the conduction band (CB) potential (−0.03 V *vs.* NHE) of BVO (Fig. S10 in Supporting information), while HOMO locates above the valence band (VB) potential of BVO (2.43 V *vs.* NHE). In this regard, electrons in the LUMO of $Au_{1-x}Pt_x$-4 NCs can readily transfer to the CB of BVO by virtue of intimate interfacial integration and suitable energy level alignment [40]. Then, the electrons flow to the photocathode to produce hydrogen and generate photocurrent, and meanwhile holes at the photoanode oxidize water to oxygen, fulfilling the PEC water oxidation reaction.

In conclusion, we elaborately engineered the $Au_{1-x}Pt_x$/BVO heterostructured by self-assembling atomically precise alloy NCs of $Au_{1-x}Pt_x$ on the $BiVO_4$ substrate under ambient conditions. It was disclosed that the $Au_{1-x}Pt_x$/BVO composite photoanodes show considerably enhanced PEC water oxidation activities and improved photo-stability compared with homogeneous Au_x NCs photosensitized BVO and pristine BVO. This is caused by the doping of hetero-atomic metallic Pt atoms on the exterior surfaces of the Au_x NCs. The synergistic action of Au and Pt atoms safeguards the gold core from rapid oxidation, enhancing photostability and accelerating surface charge transfer kinetics. Furthermore, the mechanism of PEC water oxidation facilitated by $Au_{1-x}Pt_x$/BVO heterostructures was elucidated. Our work would significantly fill the long-term blank in unlocking the charge transfer characteristic of alloy NCs for solar energy conversion.

Declaration of competing interest

The authors declare that they have no known competing financial interests or personal relationships that could have appeared to influence the work reported in this paper.

CRediT authorship contribution statement

Xian Yan: Writing – original draft. **Huawei Xie:** Software. **Gao Wu:** Investigation. **Fang-Xing Xiao:** Supervision.

Acknowledgments

The support by the award Program for Minjiang scholar professorship is greatly acknowledged. This work was financially supported by the National Natural Science Foundation of China (Nos. 21703038, 22072025). The financial support from State Key Laboratory of Structural Chemistry, Fujian Institute of Research on the Structure of Matter, Chinese Academy of Science is acknowledged (No. 20240018).

Supplementary materials

Supplementary material associated with this article can be found, in the online version, at doi:10.1016/j.cclet.2024.110279.

References

[1] Z. Luo, X. Yuan, Y. Yu, et al., J. Am. Chem. Soc. 134 (2012) 16662–16670.
[2] F.X. Xiao, S.F. Hung, J. Miao, et al., Small 11 (2015) 554–567.
[3] X. Fu, X. Lin, X. Ren, et al., Chin. Chem. Lett. 32 (2021) 565–568.
[4] Z.W. Guo, Y. Chen, Z.H. Chen, et al., Chin. Chem. Lett. 35 (2024) 109124.
[5] Q.L. Mo, X.C. Dai, Y. Xiao, et al., Chin. Chem. Lett. 34 (2023) 107901.
[6] W.D. Tian, W.D. Si, S. Havenridge, et al., Sci. Bull. 69 (2024) 40–48.
[7] H.G. Zhu, X. Yuan, Q.F. Yao, et al., Nano Energy 88 (2021) 106306.
[8] Q. Xue, Z.P. Wang, S.G. Han, et al., J. Mater. Chem. A 10 (2022) 8371.
[9] F.X. Xiao, Z. Zeng, S.H. Hsu, et al., ACS App. Mater. Interfaces 7 (2015) 28105–28109.
[10] S. Liu, Y.J. Xu, Sci. Rep. 6 (2016) 22742–22755.
[11] R. Jin, C. Zeng, M. Zhou, et al., Chem. Rev. 116 (2016) 10346–10413.

[12] H. Qian, D.E. Jiang, G. Li, et al., J. Am. Chem. Soc. 134 (2012) 16159–16162.
[13] S. Xie, H. Tsunoyama, W. Kurashige, et al., ACS Catal. 2 (2012) 1519–1523.
[14] Y. Negishi, T. Iwai, M. Ide, Chem. Commun. 46 (2010) 4713–4715.
[15] E. Gottlieb, H. Qian, R. Jin, Chem.Eur. J. 19 (2013) 4238–4243.
[16] H. Wang, J. Li, J. Chen, et al., Chin. Chem. Lett. 34 (2023) 108007.
[17] L. Peng, Y. Bian, X. Shen, et al., Chin. Chem. Lett. 31 (2020) 2871–2875.
[18] X. Zhou, C. Wang, F. Liu, et al., Chin. Chem. Lett. 32 (2021) 3261–3263.
[19] X.C. Dai, M.H. Huang, Y.B. Li, et al., J. Phys. Chem. C 124 (2020) 4989–4998.
[20] J.H. Xu, Z. Wang, W.H. Yu, et al., ChemSusChem 9 (2016) 1146–1152.
[21] K. Sheng, L.M. Fan, X.F. Tian, et al., Sci. China Chem. 63 (2020) 182–186.
[22] Q. Zhao, Z. Liu, Z. Guo, et al., Chem. Eng. J. 433 (2022) 133226–133236.
[23] J. Huang, Y. Wang, K. Chen, et al., Chin. Chem. Lett. 33 (2022) 2060–2064.
[24] Y.C. Wang, Y.Y. Liu, X.F. Huang, et al., Chin. Chem. Lett. 35 (2024) 109301.
[25] X.M. Chen, Y.Y. Wu, Y. Tang, et al., Chin. Chem. Lett. 35 (2024) 109245.
[26] X.X. Huang, Z.L. He, Y.P. Chen, et al., Chin. Chem. Lett. 35 (2024) 109271.
[27] Q. Chen, Y. Xiao, F.X. Xiao, Inorg. Chem. 63 (2024) 1471–1479.
[28] Z.Q. Wei, S. Hou, X. Lin, et al., J. Am. Chem. Soc. 142 (2020) 21899–21912.
[29] P. Yue, H. She, L. Zhang, et al., Appl. Catal. B: Environ. 286 (2021) 119875.
[30] K.R. Tolod, S. Hernandez, M. Castellino, et al., Int. J. Hydrogen Energy 45 (2020) 605–618.
[31] Y. Wang, W. Jiang, W. Yao, et al., J. Colloid Interface Sci. 590 (2021) 144–153.
[32] Z.K. Xie, H.Y. Luo, S.J. Xu, et al., Adv. Funct. Mater. 34 (2024) 2313886.
[33] Y.C. Gao, C. Wang, C.X. Zhang, et al., Microchim. Acta 188 (2021) 50.
[34] C.J. Yu, T.H. Chen, J.Y. Jiang, et al., Nanoscale 6 (2014) 9618–9624.
[35] X.Le Guevel, V. Trouillet, C. Spies, et al., J. Phys. Chem. C 116 (2012) 6047–6051.
[36] Z.Q. Wei, X.C. Dai, S. Hou, et al., J. Mater. Chem. A 8 (2020) 177–189.
[37] X.C. Dai, M.H. Huang, Y.B. Li, et al., J. Mater. Chem. A 7 (2019) 2741–2753.
[38] A. Zaban, M. Greenshtein, J. Bisquert, ChemPhysChem 4 (2003) 859–864.
[39] R. Khan, M.H. Naveen, M.A. Abbas, et al., ACS Energy Lett. 6 (2020) 24–32.
[40] X. Yan, X.Y. Fu, F.X. Xiao, Adv. Funct. Mater. 33 (2023) 2303737.